



## Experimental and numerical evaluation of the structural performance of novel S-CN connections in modular construction

Tran-Van Han <sup>a,d</sup>, MoonSook Jeong <sup>b</sup>, YongNam Kim <sup>c</sup>, Dongkyu Lee <sup>a</sup>, Nguyen Huu Cuong <sup>a,e</sup>, Kihak Lee <sup>a,\*</sup>

<sup>a</sup> Deep Learning Architecture Research Center, Department of Architectural Engineering, Sejong University, 209 Neungdong-ro, Gwangjin-gu, Seoul 05006, Republic of Korea

<sup>b</sup> Samsung C&T Corp., 26 Sangil-ro 6-gil, Gangdong-gu Seoul, Seoul 05288, Republic of Korea

<sup>c</sup> Mirae Structural Engineering Co., Ltd., 417 Daemyung Bellion, 127 Beobwon-ro, Songpa-gu, Seoul, Republic of Korea

<sup>d</sup> Faculty of Civil Engineering, Mien Trung University of Civil Engineering, Tuy Hoa and Danang, Viet Nam

<sup>e</sup> Department of Civil Engineering, Vinh University, Vinh 461010, Viet Nam

### ARTICLE INFO

#### Keywords:

Novel steel structures  
Modularized construction  
3D sand printing  
Rectangular hollow section  
Finite element analysis

### ABSTRACT

The novel S-CN (Samsung Connection Nodes) connection system, featuring nodes crafted from 3D-printed sand molds and integrated with vertical and horizontal components paired with rectangular hollow section (RHS) members, provides an effective method for connecting modules in steel modular buildings. This study employs experimental and numerical methods to assess the axial compression and tensile capacities of vertical connections, as well as the shear capacities of horizontal connections. Results show that the vertical connection's axial capacity is significantly influenced by the thickness of the roof node's top plate. While the reduction in area due to the roof node's openings affects compression performance, it has minimal impact on tensile performance. Similarly, the shear capacities of horizontal connections depend on the capacities of their shear pins. The parametric study reveals that increasing the thickness of the roof node's top plate leads to a linear increase in both the ultimate tensile and compression loads of the vertical connections. Additionally, increasing the diameter of the shear pins results in a modest increase in the ultimate shear load of the horizontal connections.

### 1. Introduction

Modular construction, a form of prefabricated building, utilizes volumetric and panelized systems. This method involves prefabricating entire building modules—such as rooms or sections—in factory-controlled environments before transporting them to construction sites for assembly [1,2]. Known for its efficiency, modular construction offers numerous benefits, including faster build times, cost reductions, improved quality control, and reduced environmental impact. As such, it is increasingly recognized as an effective solution to housing affordability issues, offering a means to quickly increase housing supply [3,4]. The effectiveness of modular construction has been demonstrated in major projects, such as the “974 Stadium” for the Qatar 2022 World Cup, constructed from 974 containers, and China’s Leishenshan Hospital, a rapid-build facility that was set up to treat COVID-19 patients, featuring 1500 beds within a 79,000 m<sup>2</sup>.

As modular construction advances into high-rise and complex structures, ensuring structural resilience, particularly under seismic conditions, is crucial. Recent research has incorporated structural health

monitoring (SHM) techniques and seismic analysis into the design of modular buildings to enhance their resistance to earthquakes [5]. SHM techniques offer a means of detecting damage and assessing the structural integrity of modular systems under seismic forces, ensuring their long-term performance.

Inter-module joining techniques are central to modular construction, governing how individual building blocks coalesce to form integrated structures [6]. Their significance becomes especially pronounced in high-rise modular buildings, which rely on the robustness of repeated module connections. Yet, one hurdle remains: the dearth of reliable and potent joining techniques, which stands in the way of modular construction’s more expansive application to high-rise buildings [7]. To address this challenge, researchers have been exploring and developing various inter-module joining techniques, which can be classified into three groups: (i) tie rod connections, (ii) bolt connections, and (iii) connector-based connection [1].

For the tie rod connection types (i), Chen et al. [8] proposed a pre-stressed modular connection, consisting of pre-stressed strands

\* Corresponding author.

E-mail address: [kihaklee@sejong.ac.kr](mailto:kihaklee@sejong.ac.kr) (K. Lee).

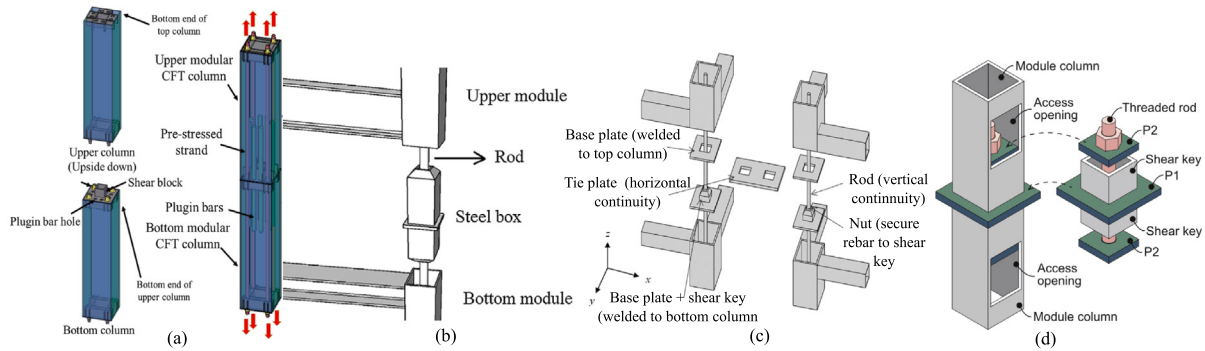


**Fig. 1.** Inter-module connections using tie rod systems studied by: (a) Chen et al. [8], (b) Sanches et al. [9], (c) Liew et al. [10], (d) Lacey et al. [12].

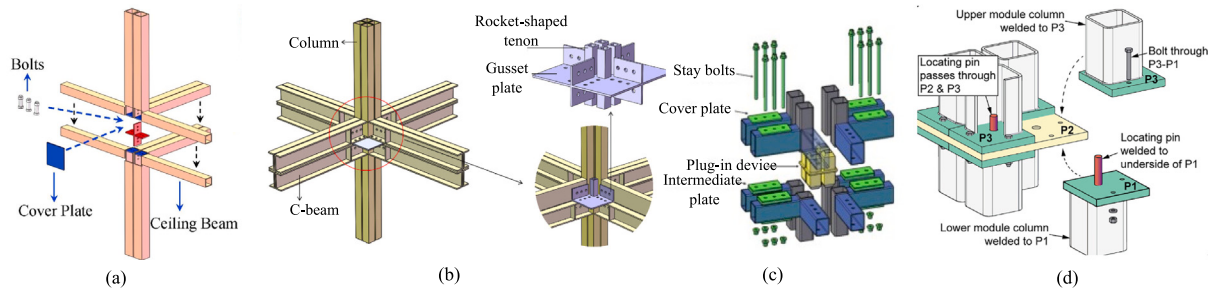


**Fig. 2.** Inter-module connections using inter-module bolt connections studied by: (a) Deng et al. [14], (b) Deng et al. [15], (c) Chen et al. [16], (d) Lacey et al. [19].

joining the modular columns vertically (see Fig. 1a). Sanches et al. [9] introduced vertical post-tensioned connections for modular steel structures, comprised of a post-tensioned threaded rod and a steel box (see Fig. 1b). Liew et al. [10] discussed a proposed method that used a gusset plate and rebar to connect adjacent modules horizontally and vertically to connect lower and upper modules (see Fig. 1c) [11]. A new post-tensioned vertical inter-module connection for modular steel buildings was proposed by Lacey et al. [12] (see Fig. 1d).

Various studies have developed (ii) inter-module bolt connection types [13]. Deng et al. [14] proposed a bolted connection with a welded cover plate for square hollow section columns (see Fig. 2a). Deng et al. [15] proposed an innovative connection for modular construction, which consists of four socket-shaped tenons and a cruciform section plate (see Fig. 2b). An innovative modular steel building connection design was presented that had an intermediate plug-in device and a beam-to-beam bolt system as the horizontal and vertical connections, respectively [16,17] (see Fig. 2c). Cho et al. [18] developed a Blind-bolted connection consisting of a number of blind and high-tension bolts to effectively connect modules. Yu and Chen [3] presented a connection type with single connecting bolts and an intermediate plate. Lacey et al. [19] introduced a novel interlocking inter-module connection which combines structural bolts with interlocking elements (see Fig. 2d). The modular joint with the connection plates was proposed by Lee et al. [20,21]. Using bolts, a connection plate and a resilient layer, Sendanayake et al. [22,23] proposed inter-modular connections that displayed superior dynamic behavior under monotonic and cyclic lateral loads, using bolts, connection plates, and a resilient layer. Sharifi et al. [24] proposed an interlocking system can be widely used in the construction of modular buildings.

The connection method using connectors (iii) is considered superior to the rod system because of its simplicity and adaptability [1]. The connectors can be welded to the columns and beams in factories, allowing for the modules to be quickly and easily connected onsite. Dhanapal et al. [25], Kalam et al. [26], Hajimohammadi et al. [27] introduced a VectorBloc connection that utilized novel cast-steel connectors and hollow structural components (see Fig. 3a). Doh et al. [28] conducted research on steel bracket connections. Chen et al. [29] investigated the

rotational rigidity of a rotary joint in a modular structural system (see Fig. 3b). Dai et al. [30] introduced novel connections known as plug-in self-lock joints that not only provided sufficient capacity but were also convenient for on-site construction (see Fig. 3c). Deng et al. [31,32,33] presented an innovative, fully prefabricated liftable connection using standard corner fittings and long stay bolts (see Fig. 3d).

Rectangular Hollow Sections (RHS) are preferred in steel constructions for their remarkable compression, torsion, and bending properties, and favorable strength-to-weight ratio [34]. Han et al. [35] recently developed an innovative method for modular construction using RHS, termed S-CN (Samsung Connection Nodes) modular steel buildings. This approach focuses on high-precision structures using a unique 3D-printed sand mold-cast connector, the S-CN connector, which incorporates vertical and horizontal connection components. In S-CN buildings, peripheral columns significantly affected by seismic loads may experience tensile and shear forces, presenting a substantial structural challenge. This study addresses these issues by conducting both experimental and numerical analyses to evaluate the compression, tensile, and shear performance of the vertical and horizontal components of the S-CN connection.

The paper is organized as follows: Section 2 introduces the concept of the S-CN connection. Section 3 and Section 4 detail the experimental programs and their results, respectively. Section 5 outlines the finite element (FE) modeling strategy and validates it against the experimental results.

## 2. The novel S-CN connection concept

A S-CN module, consisting of four RHS floor beams, four RHS roof beams, and four RHS columns, are manufactured in factories (see Fig. 4). Each module is equipped with four roof and four floor nodes at the corners. The roof modular nodes are welded to both the roof beams and the columns, and the floor modular nodes are similarly welded to the columns and floor beams.

Fig. 4 illustrates the lifting process and provides details of the modular frame utilizing S-CN connections. Notably, the liftable roof modular nodes include holes at the top designed to accommodate hoist

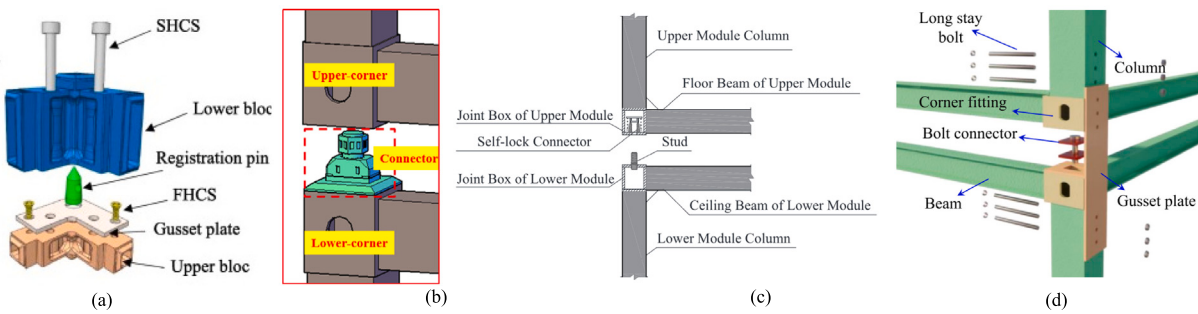


Fig. 3. Inter-module connections using connector-based connections studied by: (a) Dhanapal et al. [25], (b) Chen et al. [29], (c) Dai et al. [30], (d) Deng et al. [33].

rings, thereby facilitating the lifting and installation process. These holes also serve as anchor points for shear pins during the assembly phase.

The actual image of the S-CN connection configuration is illustrated in Fig. 5. At the construction sites, modular connections are established both horizontally and vertically using shear pins, tie plates, lower and upper sleeve joints, intermediate rods, and rods. Fig. 6 illustrates the assembly and disassembly process of the S-CN modules at the construction sites. Initially, in factories, each column is fitted with a rod and an intermediate rod, connected together using an upper sleeve joint. This upper sleeve joint is employed to keep the rods secured inside the column throughout transportation to the construction site. The assembly process of the S-CN modular system occurs in two primary steps, connecting the modules both horizontally and vertically at the construction site.

- Step 1: Horizontal connections

In this step, two modules on the same floor are connected horizontally using shear pins, lower sleeves, tie plates, and the roof nodes of both modules. First, the shear pins and lower sleeves are screwed into their respective threaded holes in the roof nodes of both modules. Once these components are secured, a tie plate with pre-drilled holes for the lower sleeves and shear pins is placed on top of the two roof nodes, aligning the components to complete the horizontal connection between the adjacent modules.

- Step 2: Vertical connections

To connect the modules vertically, a crane lifts the upper module and aligns it with the module below. The vertical connection is formed using rods, intermediate rods, upper sleeves, and lower sleeves. The rods and intermediate rods are already connected via upper sleeves and pre-installed in the RHS column during the prefabrication process. At the construction site, the pre-drilled holes in the bottom plate of the floor node in the upper module are aligned with the shear pins and lower sleeves already installed on the lower module. Finally, the rod in the upper module is screwed into the lower sleeve of the module below, completing the threaded connection and securing the vertical link between the two modules.

This S-CN connection system allows for quick and efficient assembly of modular buildings both horizontally and vertically at construction sites, eliminating the need for welding and significantly speeding up the construction process.

Compared to previous connection methods, the S-CN connection offers several advantages:

(a) Ease of hoisting: The module unit can be easily lifted using the hoist ring installed at the roof node, effectively decreasing construction time.

(b) Simple assembly and disassembly: The S-CN connection utilizes only threaded connections, eliminating the need for on-site welding

between adjacent modules and ensuring that all joints are fully prefabricated. Should there be a need to relocate and reassemble the building, the module units can be disassembled quickly, facilitating efficient recycling efforts

(c) Architectural integration: the S-CN connector integrates its components within the RHS nodes and columns, which helps maintain the building's external appearance and architectural coherence since the connectors do not protrude.

(d) Mechanical performance: the S-CN connector stands out for its ability to efficiently transmit forces. It resists compression forces using nodes, tie plates, and RHS columns, while tensile forces are managed by nodes and rods. Shear forces are addressed through the coordinated action of rods and shear pins, demonstrating the system's comprehensive mechanical capabilities.

## 2.1. Fabrication

The fabrication process of the 3D-printed nodes used in this study is illustrated in Fig. 7. Initially, sand molds are produced using 3D sand printing technology, which enables the creation of complex shapes that are difficult to achieve with conventional casting methods (Fig. 7a). These 3D-printed sand molds serve as the basis for casting the metal molds (Fig. 7b). Subsequently, the raw modular nodes are cast using these metal molds and undergo further finishing processes, including polishing and trimming, to produce the final nodes (Fig. 7c). Cold-formed RHS beams and columns are then welded to the nodes, resulting in the formation of steel modular units. These units are transported to the construction site and assembled using the S-CN connectors (Fig. 7d), finalizing the construction of the modular structure.

## 3. Experimental program

Throughout the investigation, tensile and compression tests were conducted on two full-scale vertical connection specimens subjected to axial tension and compression loads, respectively. Additionally, a shear test was conducted to evaluate the shear capacity of the horizontal connection.

### 3.1. Description of the S-CN connection's components

Experimental evaluations were conducted on full-scale vertical connection specimens subjected to compression and tensile loads, as well as on horizontal connections under shear loading. The testing apparatus was designed to replicate the axial compression loads typical of corner beam-column connections. The dimensions of the S-CN floor and roof nodes are provided in Fig. 8. The steel rod with a diameter of 22 mm and two shear pins were employed in the study. The shear pin has a thread length of 18 mm, a minor diameter of 21 mm, and a major diameter of 24 mm. The lower sleeve pin, which has a thread length of 22.5 mm, a minor diameter of 47.5 mm, and a major diameter of

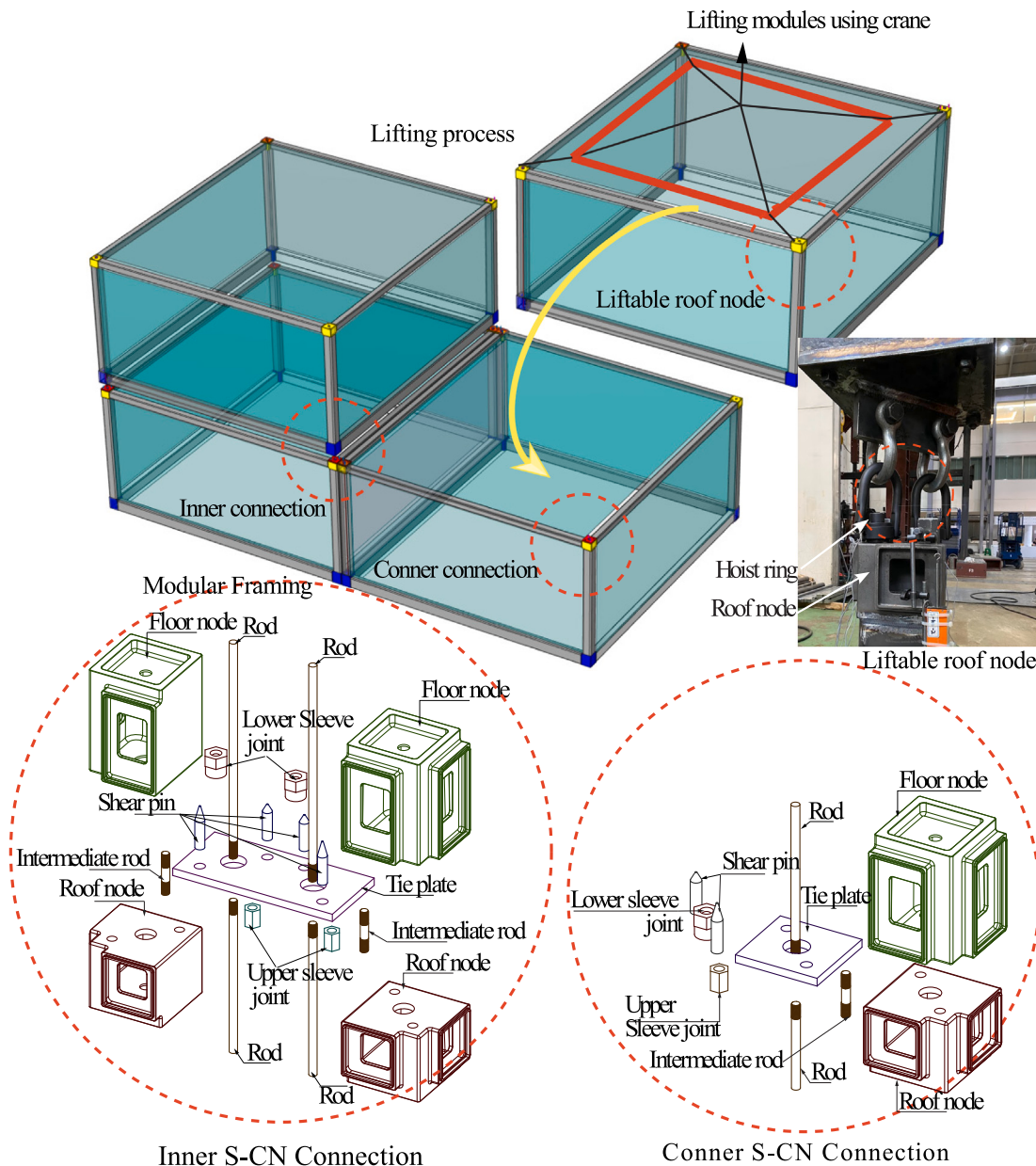


Fig. 4. The lifting process and details of the modular frame using the S-CN connections.

**Table 1**  
Geometric properties of the RHS sections.

RHS section	Width (mm)	Depth (mm)	Thickness (mm)
RHS floor beam	150	250	5
RHS roof beam	150	150	5
RHS column	200	200	10

50 mm, was used. Details are provided in Fig. 9. Key information about the geometric properties of the RHS section members, such as beams and columns, is provided in Table 1.

### 3.2. Material properties

The specimens were of the same steel grade components as the prototype structure. The unit floor and roof nodes and RHS column

were fabricated from SCW550 steel in accordance with the Korean standards, while the RHS beam members were made of S275 steel. Other components were made of S45C steel. Key information about the mechanical properties of the specimen components is given in Table 2.

### 3.3. Description of the test specimens and setup

#### 3.3.1. Vertical connection specimen under axial loads

In the S-CN modular system, the vertical connection facilitates precise vertical alignment, addressing installation tolerances that could induce unintended forces and moments within the modules. Additionally, it provides resistance to potential tensile forces in columns, especially peripheral ones, during seismic events. Throughout the investigation, two full-scale vertical connection specimens were subjected to axial tension and compression loads, respectively.

Both test configurations featured a vertical connection comprising a 54 mm diameter threaded lower sleeve joint, attached to the central

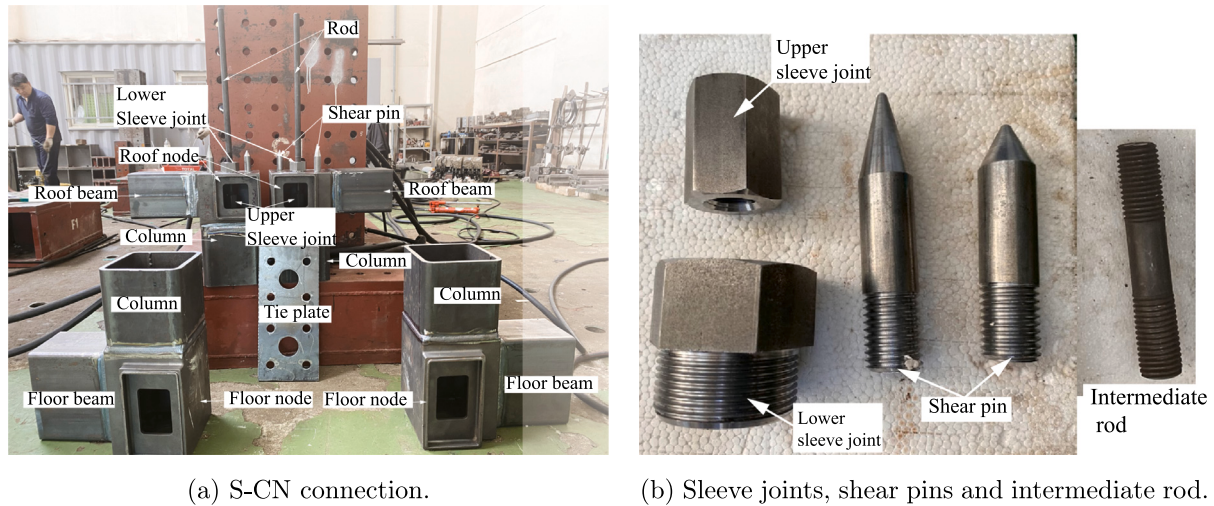


Fig. 5. The actual image of a typical S-CN connection.

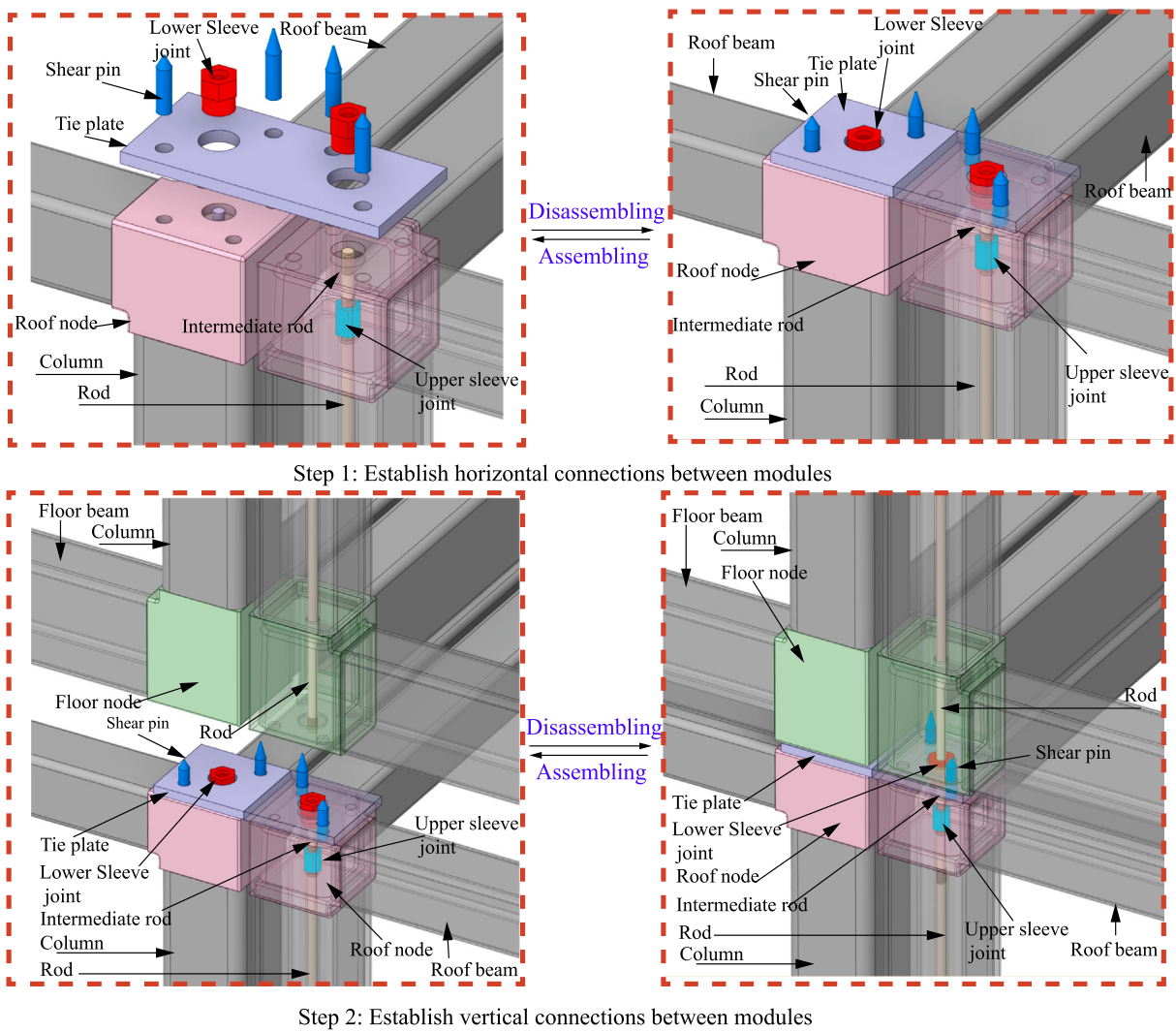
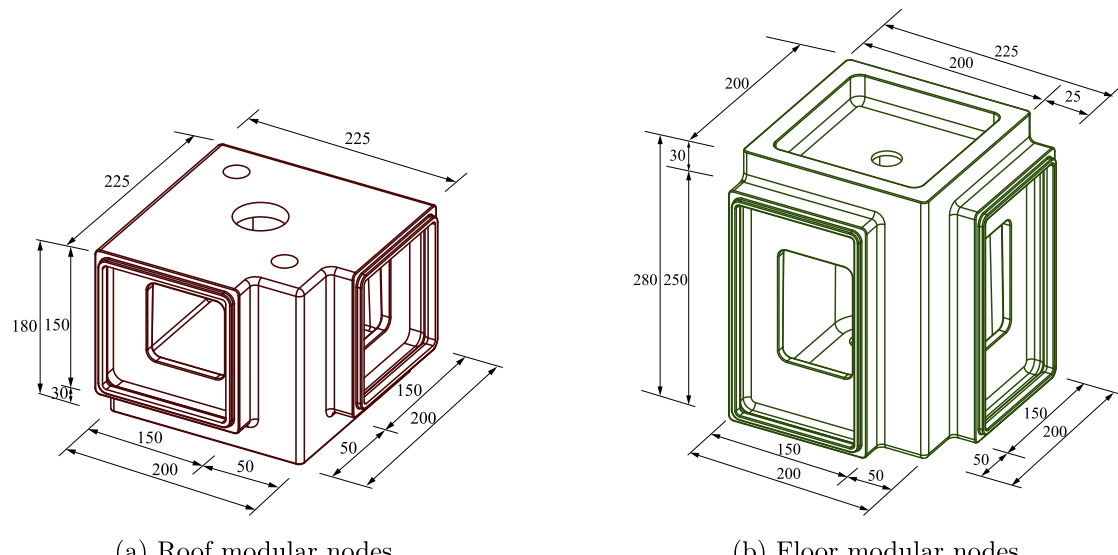


Fig. 6. The assembly and disassembly process of the S-CN modules at the construction sites.



**Fig. 7.** Fabrication process of the modular nodes (a) 3D-sand printed mold; (b) metal casting mold (c) raw nodes; (d) S-CN connections.



**Fig. 8.** Dimensions of floor modular nodes and roof modular nodes.

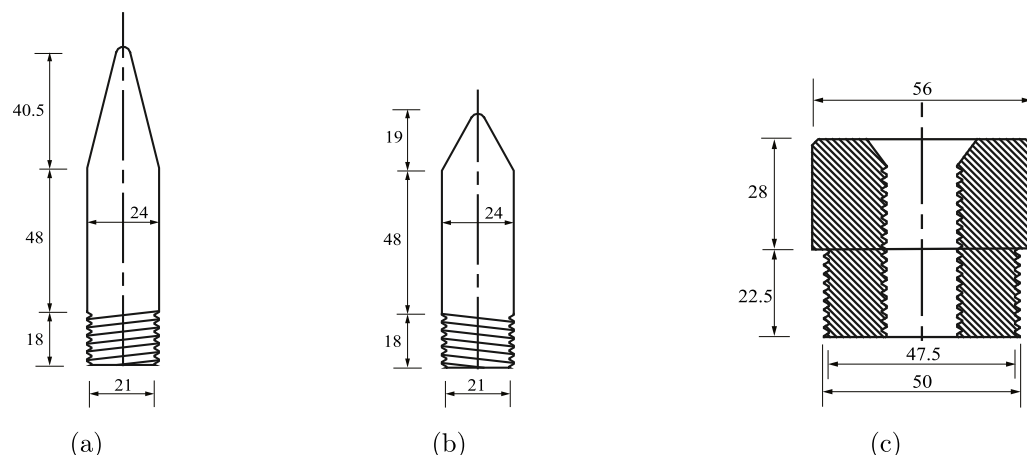
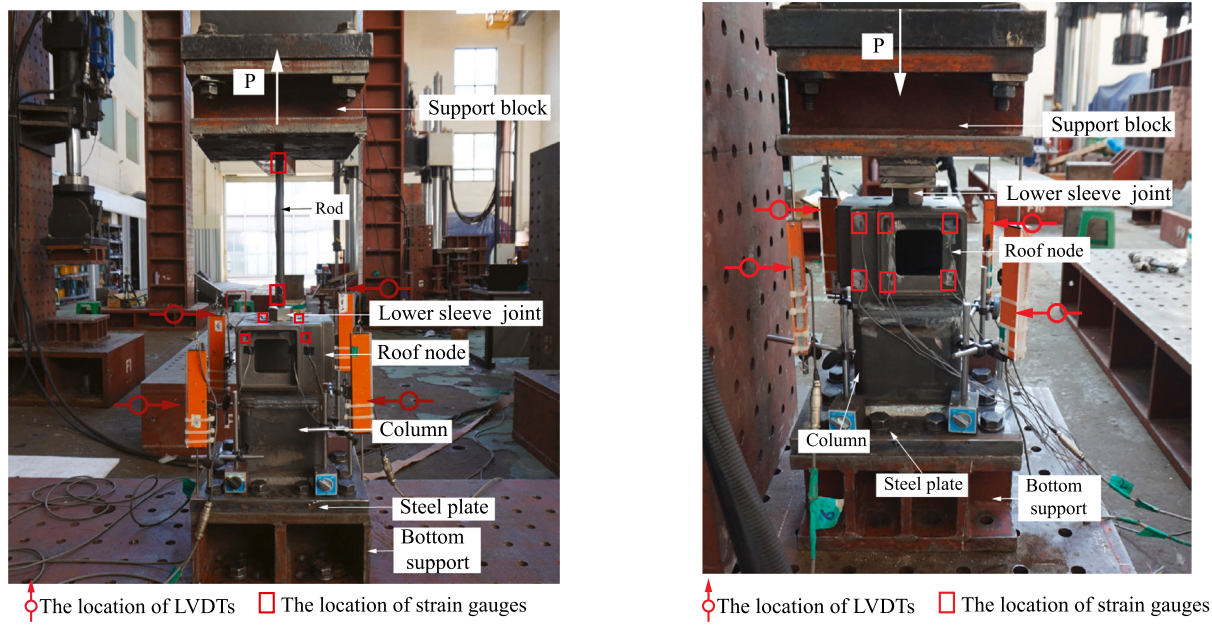


**Fig. 9.** Cross-section of (a) the long shear pin; (b) the short shear pin and; (c) the lower sleeve .

**Table 2**  
Mechanical properties of the specimen components.

Component	Material specification	Young's modulus (E) (GPa)	Yield strength ( $F_y$ ) (MPa)	Ultimate strength ( $F_u$ ) (MPa)
Floor and roof nodes	SCW550	205	509	649
RHS floor and roof beams	S275	203	275	430
RHS column	SCW550	205	509	649
Tie plate	S45C	205	490	686
Lower and upper sleeve joint	S45C	205	490	686
Rod and intermediate rod	S45C	205	490	686
Shear pin	S45C	205	490	686



(a) Tensile test.

(b) Compressive test.

**Fig. 10.** The test set-up of the vertical connection specimens under axial tension load and compression load.

threaded hole at the top of the roof node. The roof node was welded to a RHS steel column, which in turn was anchored to the foundation via bolted connections on a base plate. For the tensile test setup, illustrated in Fig. 10(a), the specimen utilized a 20 mm diameter, 500 mm long rod threaded into the lower sleeve, with the upper end secured to a support block using nuts. In the compression test, as depicted in Fig. 10(b), a shorter 130 mm rod was employed to facilitate the direct application of compressive loads onto the lower sleeve, with a similar attachment to the roof node and support block.

The loading program for both tests involved the application of axial loads using a 10,000 kN actuator mounted within a rigid steel frame. Axial loads were applied in displacement-controlled mode at a constant rate of 2.5 mm/min, progressively increasing until failure. In the tensile test, the axial load was applied at the top of the rod, transferring through the lower sleeve, while in the compression test, the load was applied directly onto the lower sleeve.

Instrumentation included a force sensor connected to the actuator to record the applied axial loads. Four Linear Variable Differential Transducers (LVDTs) were positioned to monitor the relative vertical displacement between the support block and the base plate. The tensile specimen was instrumented with 11 strain gauges (G1 to G4 placed around the center hole of the roof node, G5 to G6 located on the rod, and G7 to G11 on the side plates of the roof node), while the compression specimen was fitted with 10 strain gauges (G1 to G10 positioned on the side plates of the roof node) to capture strain variations during loading. The experimental setup and instrumentation for both tests are shown in Fig. 11a-b.

### 3.3.2. Horizontal connection specimen under shear load

In this study, the shear capacity of the horizontal connection between the upper and lower modules in the S-CN system was evaluated. The upper module consisted of a modular floor node, an RHS column, and an RHS beam, while the lower module was simplified to a modular roof node and an RHS beam. The connections between the nodes and RHS sections were established using single J-groove welds. The upper and lower modules were connected through a tie plate, two shear pins, and a lower sleeve joint threaded into the roof node. Additionally, a rod inside the RHS column of the upper module was threaded into the lower sleeve and secured at the top with nuts. The shear capacity was

assessed by fixing the lower module and applying lateral load to the upper module until the horizontal connection failed. The test set-up was depicted in Fig. 12.

The test setup utilized a 10,000 kN load actuator positioned horizontally within a steel frame to apply the shear load ( $P_1$ ). This load was transmitted through support plate 1 to the floor beam and the floor node of the upper module. Simultaneously, the roof beam of the lower module was connected to support plate 2, which was firmly held by a stiff frame to prevent movement. To ensure proper alignment with the stiff frame, the lower module was rotated 180 degrees around the y-axis from its original design, allowing its RHS beam to face the stiff frame, ensuring secure fixation during testing. The shear load was applied at a constant rate of 2.5 mm/min, and loading continued incrementally until failure occurred. An additional axial load ( $P_2$ ), equal to 5% of the RHS column's compressive buckling strength, was applied, corresponding to a force of 106 kN [36].

Five LVDTs (D1-D5) were attached to the test specimen for precise displacement measurements. LVDTs D1, D2, and D5 measured the relative displacement between the two support plates connected to the floor and roof beams, and the base. Simultaneously, D3 and D4 were used to gauge the relative displacement between the support plate and the tie plate.

## 4. Test results and discussion

### 4.1. Vertical connection specimen under axial tension and compression loads

The compression load was applied using the displacement control method, and the vertical connection specimens were loaded until a considerable decline in load after reaching the ultimate load ( $P_u$ ) was observed. The displacement of the loading plate was calculated by averaging the displacement results measured by the LVDTs installed in the experiments.

The load-deformation response of the specimen under axial tension is depicted in Fig. 13(a). It reveals that the connector specimen reached a peak load of 290.74 kN. Following this peak, there was a noticeable decrease in load capacity, which was attributed to deformations at the

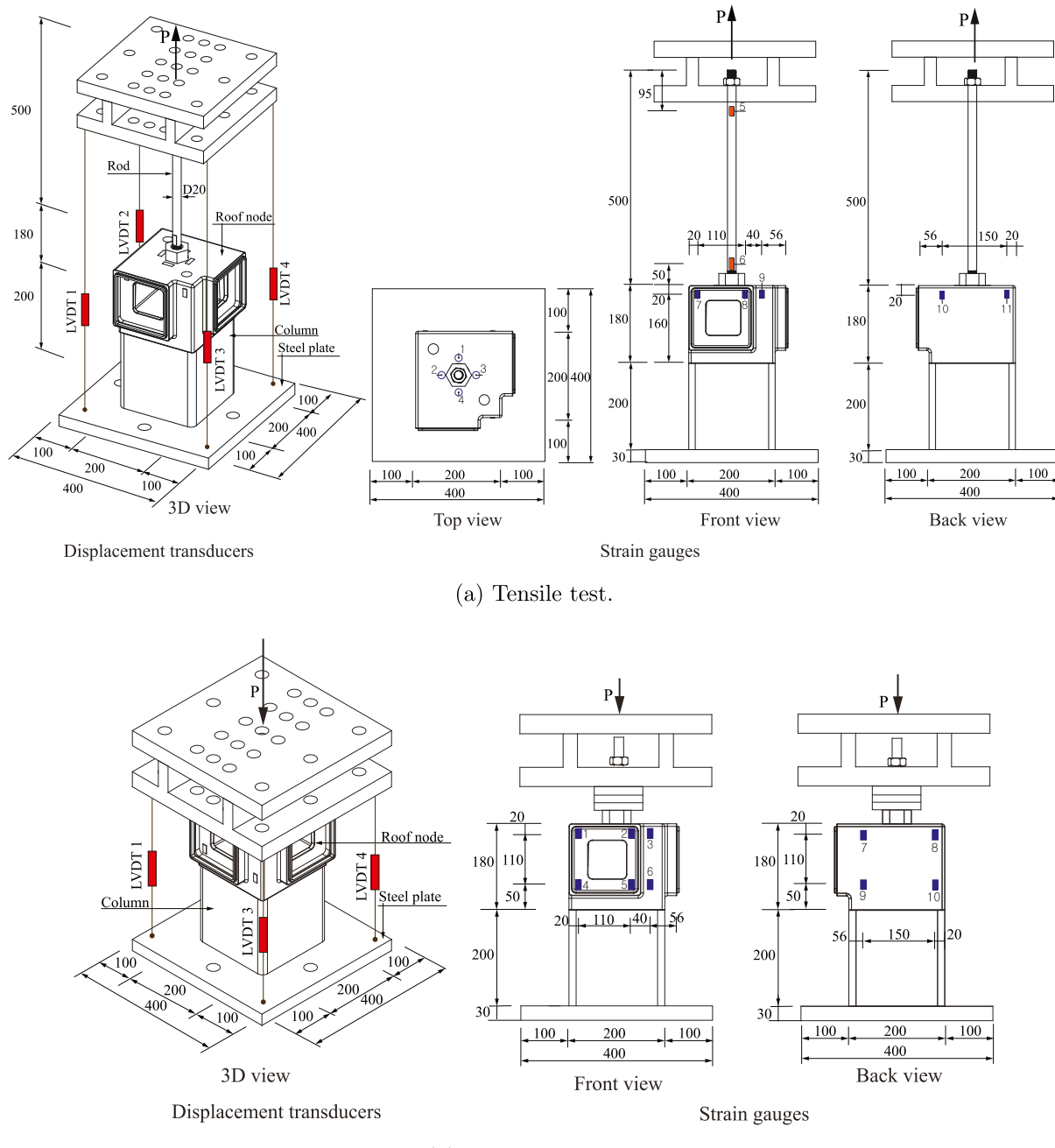
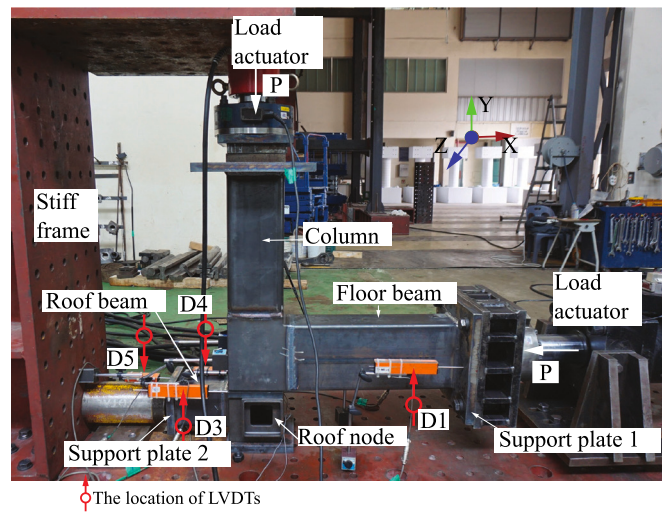


Fig. 11. Arrangement of the transducers for axial compressive and tensile tests on the vertical connection specimens.

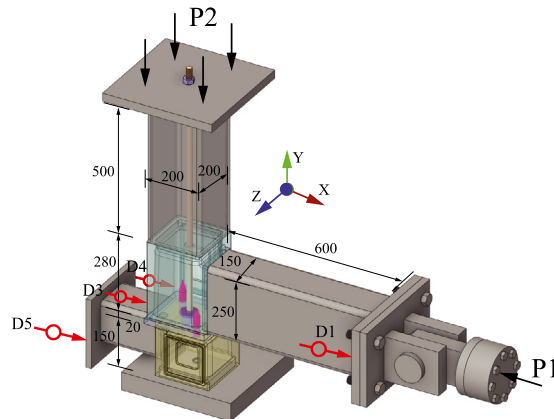
upper roof node and the consequent detachment of the lower sleeve from this node.

Figs. 14 and 13(b) display the maximum strain values at various locations at the ultimate load of the specimen under tensile load and compare them with the yield strain  $\epsilon_{y-Node}$  and ultimate strain  $\epsilon_{u-Node}$  values. As depicted in Fig. 14a, the strain values on the top plate of the roof node (G1–G4) were the highest observed. Specifically, strain values for G1 and G2, located on the side without openings, were significantly higher – ranging between 1.55 and 1.75 times – compared to G3 and G4 on the side with openings. These strain values for G1–G4 not only exceeded the yield strain  $\epsilon_{y-Node}$  but were also considerably lower than the ultimate strain  $\epsilon_{u-Node}$  of 0.12943 mm/mm. This indicates that the failure of the roof node was not due to material failure, consistent with observations in Fig. 15.

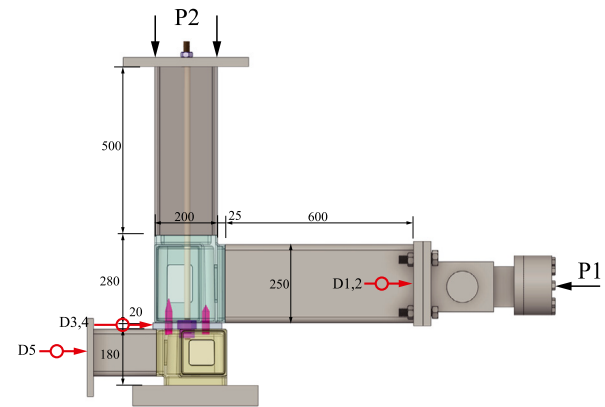
In Fig. 14(b,c), strain measurements on the roof node's side wall for G7 to G9 on the front view and G10 to G11 on the back view were negative due to bending of the top plate of the roof node. Notably, only G8, positioned near the opening, recorded a strain exceeding the yield strain  $\epsilon_{y-Node}$  by 0.15%, suggesting that the openings marginally reduce the tensile capacity of the specimen, while the side wall thickness plays a negligible role in its tensile performance. Additionally, Fig. 14b shows that strain values on the rod surpassed the yield strain  $\epsilon_{y-Node}$  of 0.0017 mm/mm, but these values were significantly lower-ranging from 2.5 to 8.56 times-compared to the strain on the top plate's roof node (G1 to G4). These findings indicate that the tensile ultimate load of the vertical connection specimen was primarily influenced by the thickness of the top plate of the roof node, rather than by the roof node walls or rod elements.



(a) The actual image of the test.

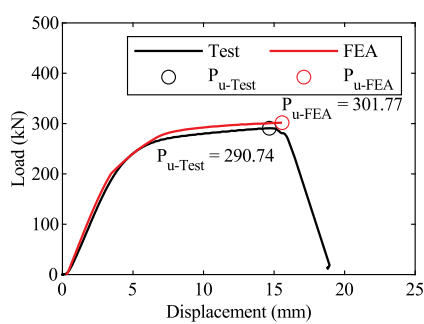


(b) 3D view.

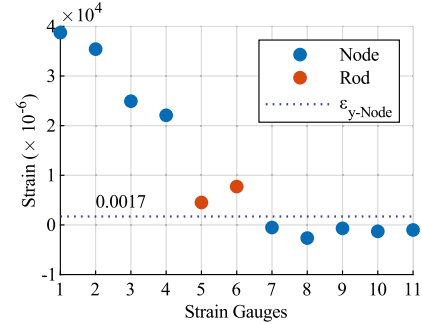


(c) Front view.

Fig. 12. The test set-up of the horizontal connection specimen under shear load.



(a) Load-deformation behavior



(b) All strain data obtained from the test

Fig. 13. Axial tension test and finite element analysis (FEA) results of the vertical connection specimen.

As illustrated in Fig. 15, once the ultimate load was reached, the specimen underwent a reduction in load capacity. This decrease was linked to local plastic deformation of the hole, resulting from bending in the upper roof node. This deformation caused a detachment in the

threaded connection between the sleeve and the hole, leading to the sleeve disengaging from the hole. This event ultimately resulted in the specimen's failure, which is characterized as a pull-out failure of the sleeve from the roof node.

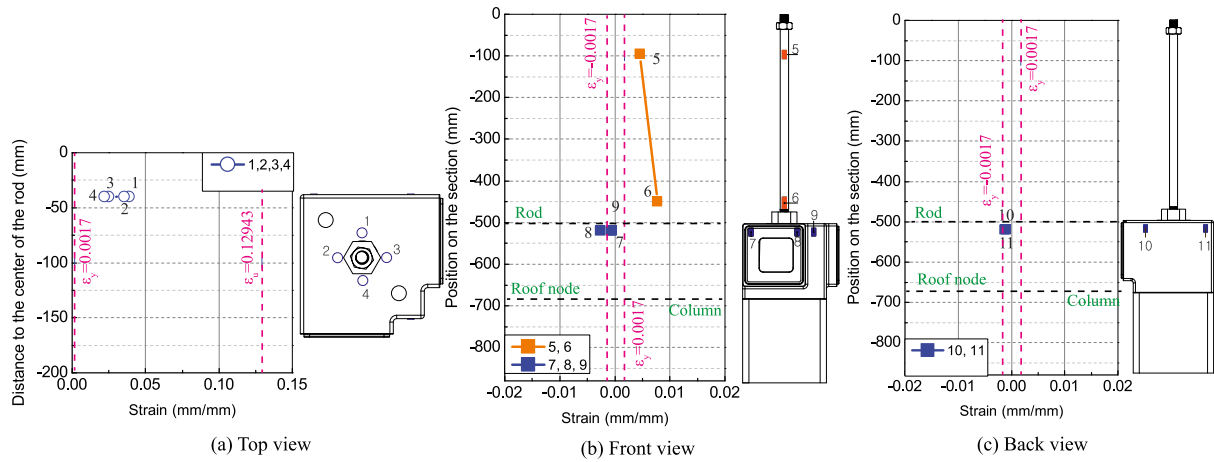


**Fig. 14.** Comparison of the strain values at various locations of the vertical connection specimen under tensile load.

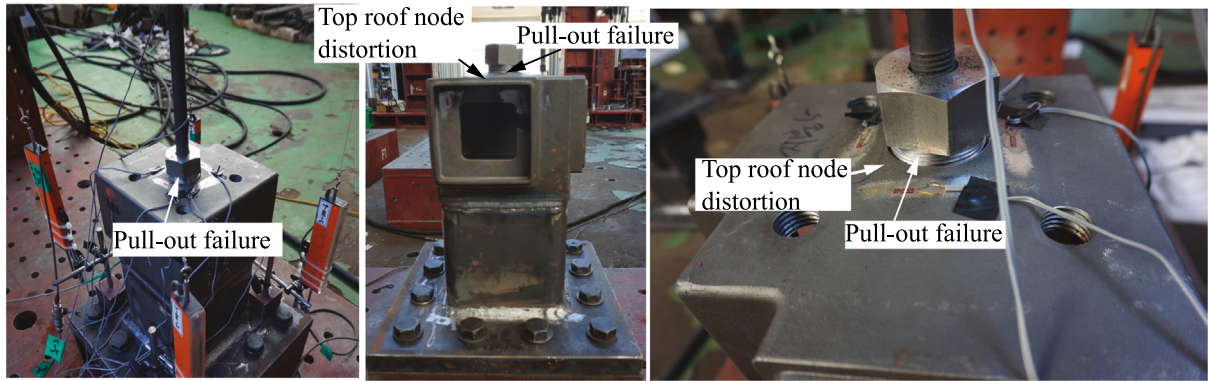


**Fig. 15.** The failure mode of the vertical connection specimen under tension load.

**Fig. 16(a)** illustrates the axial compressive load-strain behavior of the specimen, revealing the vertical connection component specimen reaching a maximum load of 290.74 kN. Immediately following the attainment of the maximum load, the load capacity of the specimen experienced a sudden drop due to severe deformation of the top roof node and the deep penetration of the lower sleeve into the roof node.

Figs. 17 and 16(b) show the maximum strain values at various locations at the ultimate load of the specimen under compression load and compare them with the yield strain  $\varepsilon_{y-Node}$  value. As depicted in **Fig. 17(a,b)**, the strain values at the upper roof node (G1, G2, G3, G7, and G8) were positive, while those at the lower roof node (G4, G5, G6, G9, and G10) were negative, attributable to the bending of the roof node's walls. The strain values at locations G1-G2 and G7-G8 exceeded the yield strain  $\varepsilon_{y-Node}$  of 0.0017 mm/mm. Notably, the strain values at location G2, located near the opening, were significantly higher than those at other node wall locations. This observation suggests that the reduction in area due to the openings resulted in stress concentration within the node section when the specimen was subjected to compression.

The post-failure state of the test specimen is illustrated in **Fig. 18**. The hole at the top of the casting node experienced deformation, and the continued pushing of the lower sleeve through the hole resulted in a substantially reduced load [37]. The bending of the top of the roof node, coupled with the sleeve's penetration of the hole, led to the detachment of the thread between the lower sleeve and the hole, ultimately causing a push-through failure of the connection. As a result, the test observations indicate that the compression performance of the specimen was influenced by the thickness of the roof node's top plate.

#### 4.2. Horizontal connection specimen under shear load

In **Fig. 19**, it is observed that the connection specimen reached an ultimate load of 316.48 kN. Once this load was achieved, there was a rapid decline in the load capacity due to the shear failure of the pins.

The post-failure state of the test specimen is depicted in **Fig. 20**. In the analysis of the two failed shear pins, it was noted that their fracture surfaces exhibited a flat morphology, primarily within the working threads of the shear pin. This specific location of fracture can be attributed to increased stress concentration. Additionally, these areas endured peak composite stress as they were the interface points where the shear pins connected with the tie plate and the roof node. Furthermore, the bottom plate of the floor node underwent deformation due to the horizontal load from the sleeve and rod, indicating the significant role they play in bearing the shear load of the S-CN connection.

#### 5. Finite element analysis

The physical testing of the specimens offered critical insights into the assembly and shear behavior of the full S-CN connection, as well as the tension and compressive behaviors of the vertical connection of S-CN. Nevertheless, these tests were limited in revealing essential details such as the region of maximum stress, variations in stress across the specimen, and the load level at which plastic strain initiates. To address these gaps, three-dimensional FE models of the horizontal and vertical connection specimens tested in this study were developed. These models were constructed using the commercially available FE software, ANSYS Mechanical Enterprise 2021/R1 [38]. Non-linear equilibrium equations were addressed via the Static Structural module. The Full

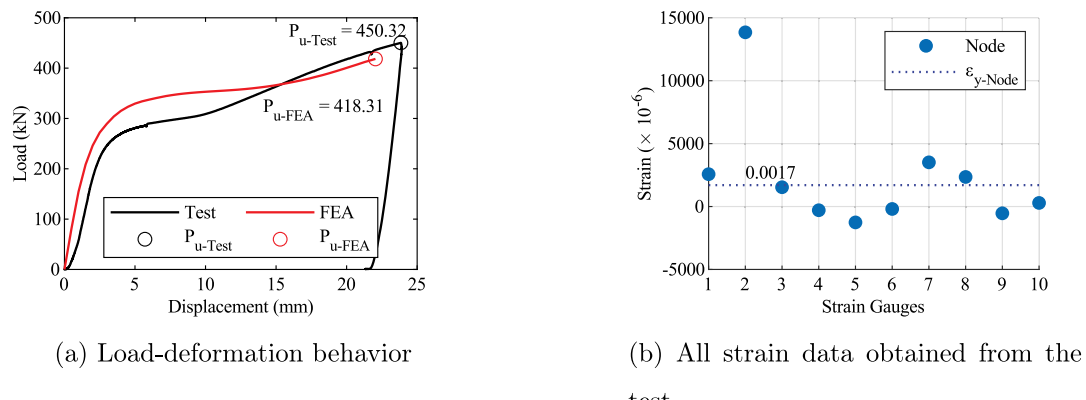


**Fig. 16.** Compression test and FEA results of the vertical connection specimen.

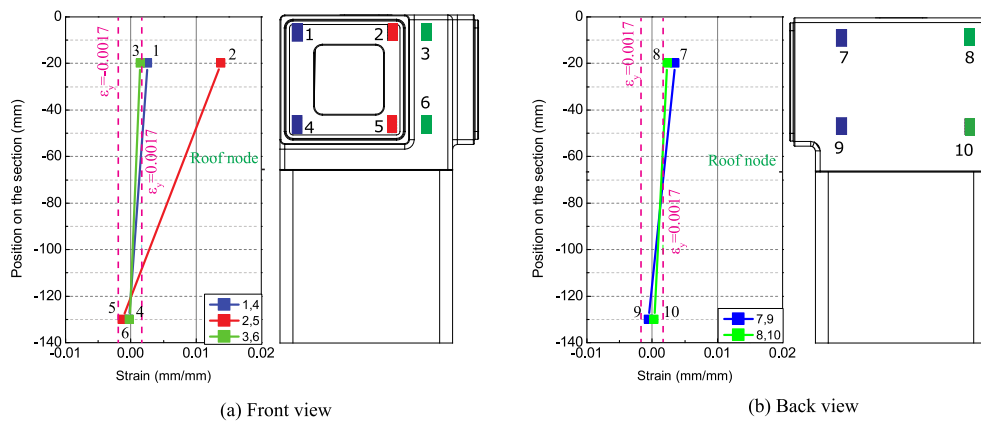


**Fig. 17.** Comparison of the strain values at various locations of the vertical connection specimen under compression load.

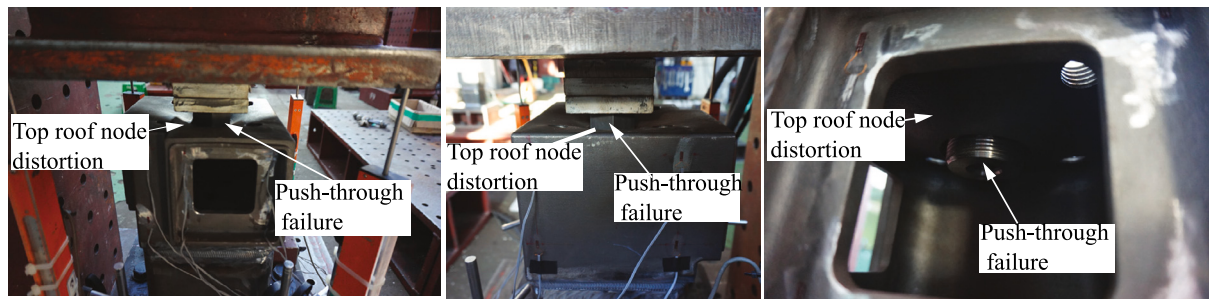


**Fig. 18.** The failure mode of the vertical connection specimen under axial compression load.

Newton–Raphson method was chosen for solution, incorporating an auto-incrementation for load application. The initial increment size was set to 0.5 mm, with minimum and maximum values of 0.05 mm and 0.5 mm, respectively. Large deflection considerations were activated during analysis. Their purpose was to provide a comprehensive understanding of the structural behavior of the connection under axial and shear loads.

### 5.1. Material models

The engineering stress–strain relationship obtained from the tensile tests of the steels in this study is described using the bilinear plus nonlinear hardening model proposed by Yun and Gardner [39]. The choice of this model was influenced by the absence of additional tensile tests, highlighting the need for a suitable approach to accurately characterize the steel's behavior.

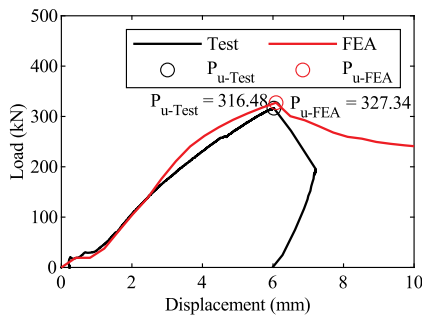


Fig. 19. Shear test and FEA results of the horizontal connection specimen.

The bilinear plus nonlinear hardening model:

$$\sigma(\varepsilon) = \begin{cases} E\varepsilon & \text{for } \varepsilon \leq \varepsilon_y \\ F_y & \text{for } \varepsilon_y < \varepsilon \leq \varepsilon_{sh} \\ F_y + (F_u - F_y) \left\{ 0.4 \left( \frac{\varepsilon - \varepsilon_{sh}}{\varepsilon_u - \varepsilon_{sh}} \right) + 2 \left( \frac{\varepsilon - \varepsilon_{sh}}{\varepsilon_u - \varepsilon_{sh}} \right)^5 \right\} & \text{for } \varepsilon_{sh} < \varepsilon \leq \varepsilon_u \end{cases} \quad (1)$$

$$\varepsilon_u = 0.6 \left( 1 - \frac{F_y}{F_u} \right) \quad (2)$$

But  $\varepsilon_u \geq 0.06$  for hot-rolled steels

$$\varepsilon_{sh} = 0.1 \frac{F_y}{F_u} - 0.055 \quad (3)$$

But  $0.015 \leq \varepsilon_{sh} \leq 0.03$

Where:  $E$  - Young's modulus;  $F_y$  - yield stress and the corresponding yield strain  $\varepsilon_y$ ;  $\varepsilon_{sh}$  - strain hardening strain;  $F_u$  - the ultimate tensile stress and the corresponding ultimate tensile strain  $\varepsilon_u$  [40].

The stress and strain obtained by the tensile test are transformed into the true stress and strain using the following equation [41]:

$$\sigma_{true} = \sigma(1 + \varepsilon) \quad (4)$$

$$\varepsilon_{true} = \ln(1 + \varepsilon) \quad (5)$$

Fig. 21 illustrates the stress-strain relationships obtained from the engineering and true stress-strain curves that were used in the FE simulations.

The Von Mises yield criterion, integrated with the Multilinear Isotropic Hardening material model [42] and isotropic strain hardening, was employed. Stress-strain relationship defining points were informed by Table 2 and Fig. 21. The input generation program for the ANSYS Multi-Linear Isotropic Hardening Model is detailed in Appendix.

## 5.2. Modeling assumption

### 5.2.1. Vertical connection specimens under axial tension and compression loads

The FE model dimensions were derived from the test specimens. The modeling of the vertical connection specimen under axial tension load in ANSYS is depicted in Fig. 22, while Fig. 23 illustrates the FE model employed for studying the specimen under axial compression load. To optimize analysis capabilities and reduce analysis time, the shape of the roof node was simplified. However, to more accurately describe the compressive and tensile behavior, as well as the failure of the vertical connection specimens, the lower sleeve was modeled in detail with its threads.

The RHS column was modeled using the four-node element, SHELL181, which has six degrees of freedom at each node. The base plate was considered rigid to negate deformations during simulations, simplifying

the analysis. Meanwhile, other components were modeled with 3D 20-node solid elements, SOLID186 [43].

The mesh sizes were determined based on the dimensions and behavior of each component under load to balance accuracy and computational efficiency. Finer mesh sizes were applied to regions with higher stress concentrations and where significant deformations or interactions were expected, such as the shear pin, threaded connections, and interfaces between components. For the vertical connection, the mesh was refined based on observed failures, particularly at the threaded connection on the top of the roof node and the pull-out failure of the lower sleeve during testing. Following a similar approach to Han et al. [35], the threads of the lower sleeve and the center hole of the roof node were meshed more finely at 1 mm to accurately capture the sliding interaction. The lower sleeve was meshed with a finer size of 3 mm, while a 5 mm mesh was used for the rod, roof node, and RHS column.

Contact interfaces between the components of the specimens were defined using CONTA174 and TARGE170 elements. A friction coefficient of 0.30 was established for steel part interfaces, specifically between the lower sleeve and the roof node, in line with EN 1090 - 2 standards [44]. This frictional behavior plays a significant role in influencing the thread failure strength [45,46]. However, the effects of varying the friction coefficient were not investigated in this study. Bonded contact was employed for surfaces between the modular nodes and RHS column, the lower sleeve and rod, and the roof node and base plate. The bottom of the base plate was fixed to ensure stability of the specimen. A displacement-controlled approach was adopted, with test displacements extending up to 25 mm.

### 5.2.2. Horizontal connection specimen under shear load

Fig. 24 describes the FE model used to study the structural behavior of a horizontal specimen under compressive and shear loads. The shapes of the roof node, floor node, and shear pins were simplified for computational efficiency. The RHS column and RHS floor beam were represented using the four-node SHELL181 elements. To ensure analytical simplicity, both the base and loading plates were treated as rigid bodies, effectively negating deformations during the simulations. All other components were modeled using 3D 20-node solid elements, SOLID186 [43].

Based on the study by Han et al. [35] and experimental observations of shear pin fracture and significant deformations at the floor node, roof node, rod, tie plate and lower sleeve, a mesh size of 5 mm was applied to these components. A coarser mesh of 10 mm was used for the RHS column, floor beam, and roof beam.

Interfaces between the various specimen components were defined using the CONTA174 and TARGE170 elements. For the steel part interfaces, which include connections between the shear pins and tie plate, the shear pin and floor node, and the lower sleeve and roof node, a friction coefficient of 0.30 was adopted in line with the EN 1090 - 2 standards [44]. Bonded contact assumptions were made for surfaces interfacing the modular nodes with the RHS column, shear pins with the roof node, the lower sleeve with the rod, the roof node with the RHS roof beam, and the roof node with the base plate. To guarantee the stability of the specimen during simulations, the bottom of the base plate was fixed. A displacement-controlled approach was adopted horizontally for the RHS floor beam, with displacements reaching up to 7 mm. Additionally, a load-controlled approach was implemented vertically at the top of the loading plate, with a compressive load of 106 kN.

## 5.3. Validation

### 5.3.1. Vertical connection specimen under axial tension and compression loads

Fig. 13(a) and Fig. 16(a) depict the comparison between the load-deformation relationships from the test and FEA results for vertical

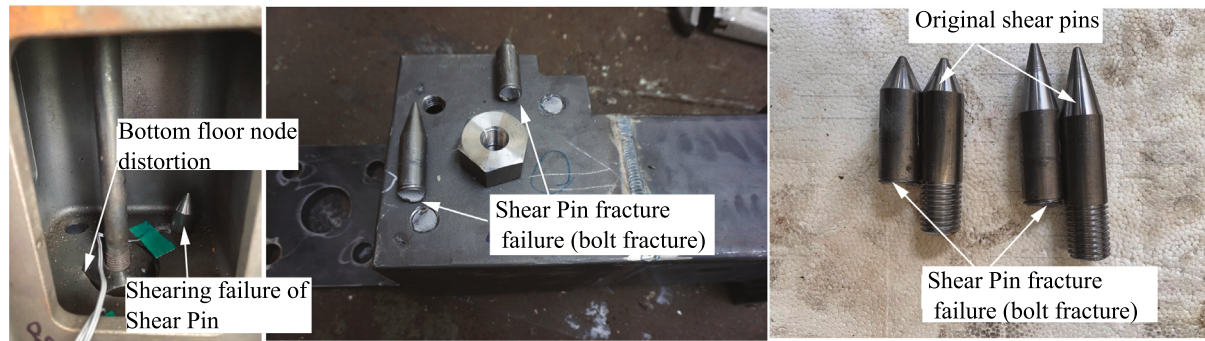


Fig. 20. Failure modes of the connection specimen under shear load.

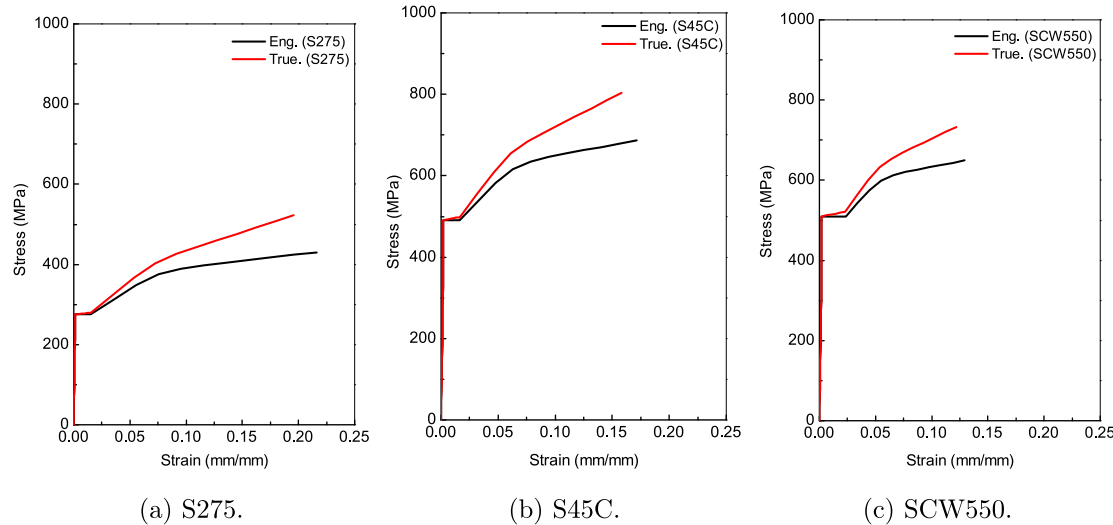


Fig. 21. Engineering and true stress-strain curves.

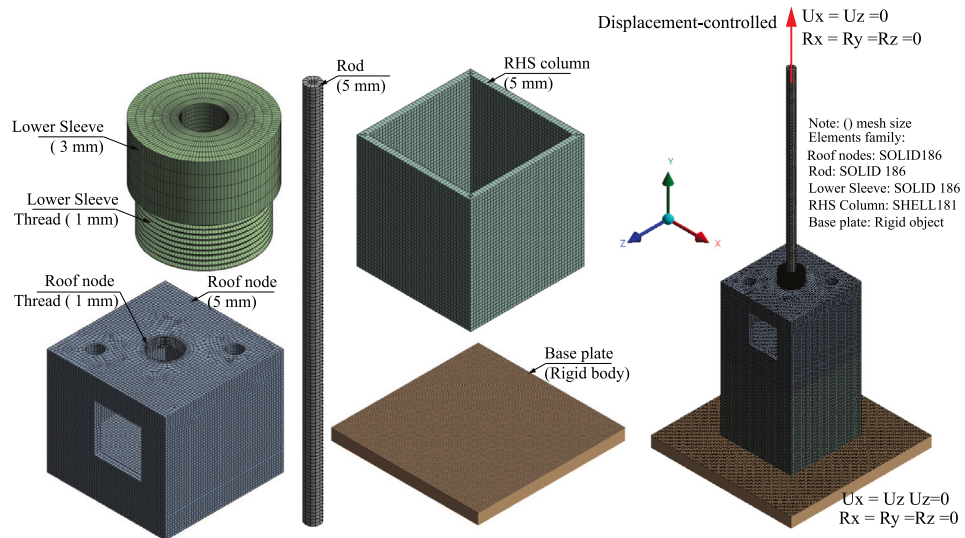


Fig. 22. FE model of the vertical connection specimen under axial tension load.

connection specimens under axial tension and compression loads, respectively. Results for Von-Mises stresses and failure modes at the peak point are shown in Fig. 25(a-b). Agreement between the analyses and tests varied among the specimens.

Vertical connection specimen under axial tension load:

- For the vertical connection specimen under axial tension load, as shown in Fig. 13(a), the FE analysis closely aligned with the experimental results. Both the test and FEA curves depicting the load-deformation relationship were almost identical. The FE model predicted an ultimate tension load of 301.77 kN, whereas

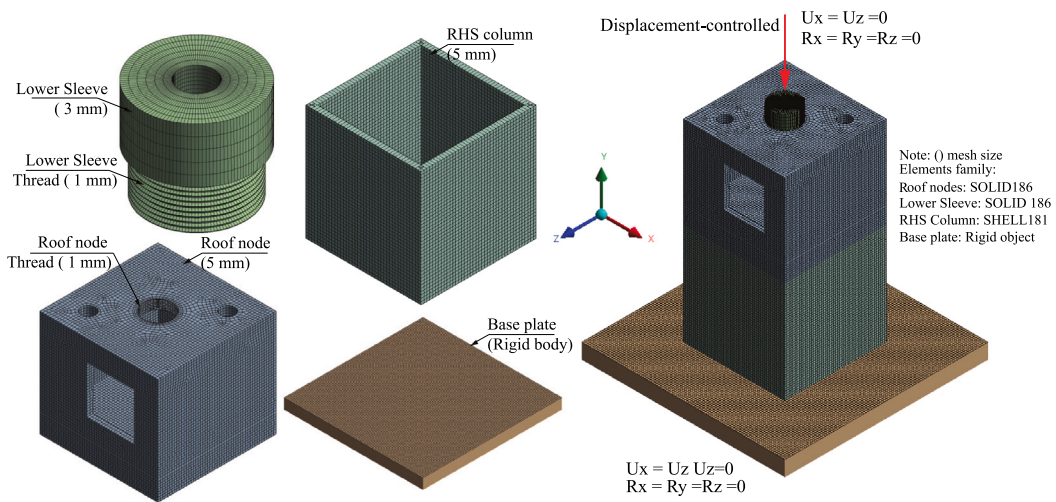


Fig. 23. FE model of the vertical connection specimen under axial compression load.

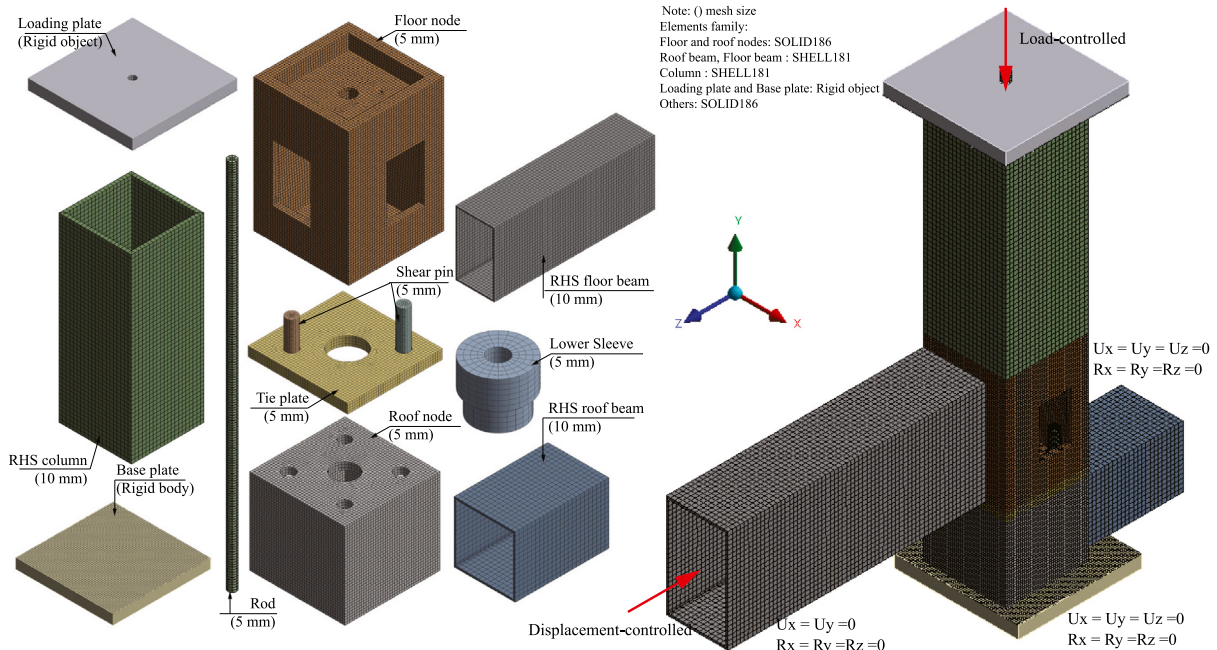


Fig. 24. FE model of the horizontal connection specimen.

the experimental value was 290.74 kN, a difference of approximately 3.8%. The displacement value at which the specimen failed in the experimental results was 14.66 mm, while the corresponding value in the FEA results was 15.57 mm, a difference of only about 6.2%.

- The failure mode is a critical evaluation criterion for the FEM. Figs. 15 and 25(a) compare the failure modes observed in experimental tests and FEA for the vertical connection specimen under axial tension load. For the lower sleeve thread connections, the Von Mises stress predicted by FEA, depicted through a color spectrum, was below the material's yield limit of 490 MPa, consistent with the experimental results. The stress in the rod exceeded the yield limit of 490 MPa, as indicated by the grey areas in the FEA, matching strain gauge readings from G5 and G6 (see Fig. 14). At the side plates of the roof node, FEA predicted stress values

ranging from 400 MPa to the yield stress of 509 MPa (orange), and above 509 MPa (grey), aligning with strain gauge readings from G7 to G11 (see Fig. 14). The grey color observed on the top plate of the roof node around the threaded hole indicated plastic deformation, confirmed by strain gauges G1 to G4. The grey color observed on the top plate of the roof node around the threaded hole indicated plastic deformation, confirmed by strain gauges G1 to G4. The predicted failure mode, involving thread detachment at the hole and pull-out failure of the lower sleeve (Fig. 25(a)), was consistent with the experimental observations.

#### Vertical connection specimen under compression load:

- For the vertical connection specimen under axial compression load, as depicted in Fig. 16(a), the FE analysis closely aligned with the experimental results. Both the test and FEA curves illustrating

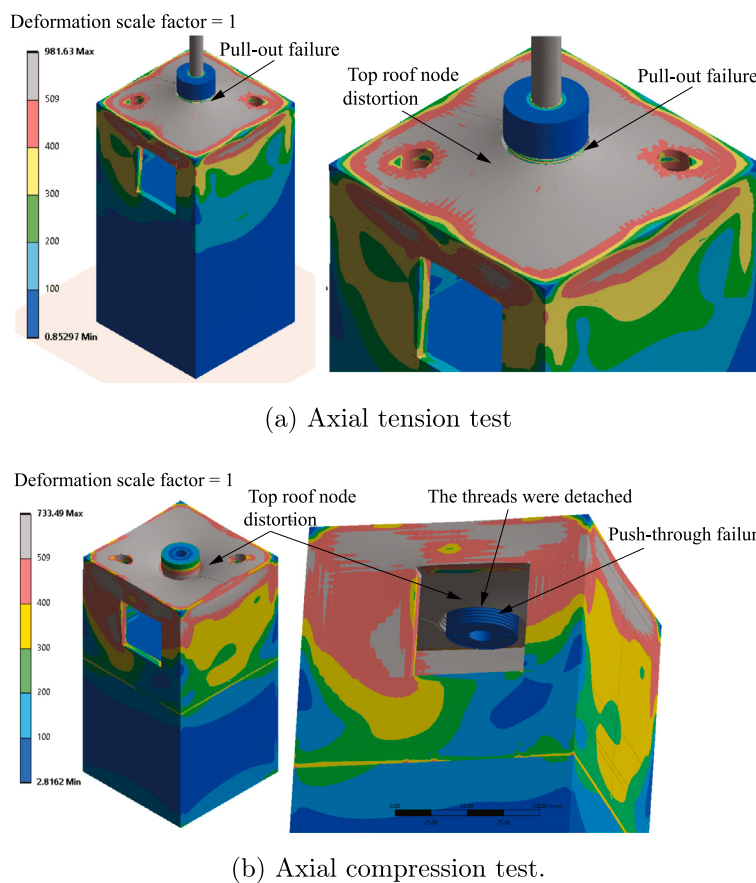


**Fig. 25.** FEA results of Von-Mises stresses and failure modes at the peak point of: (a) axial tension test; (b) axial compression test.

the load-deformation relationship were well matched. The FE model predicted an ultimate compression load of 418.31 kN, while the experimental value was 450.32 kN, a difference of approximately 7.7%. The displacement value at which the specimen failed in the experimental results was 23.85 mm, whereas the corresponding value in the FEA results was 22.04 mm, a difference of about 8.2%.

- **Figs. 18 and 25(b)** compare the failure modes from experimental tests and FEA for the vertical connection specimen under axial compression load. The Von Mises stress predicted by FEA for the lower sleeve remained within the elastic range consistent with experimental results. At the roof node's side plates near strain gauges G1, G2, G3, G7, and G8, FEA indicated stress levels between 400 MPa and the yield stress of 509 MPa (orange) and exceeding 509 MPa (grey), aligning with strain gauge measurements (**Fig. 17**). In the lower section of the roof node near gauges G4 to G6 and G9 to G10, FEA predicted stress levels below 400 MPa (blue, light blue, green, and yellow), within the elastic limit, as confirmed by strain gauges. The FEA-predicted failure mode, involving pull-through and detachment of the lower sleeve (**Fig. 25(b)**), closely matched experimental observations.

### 5.3.2. Horizontal connection specimen under shear load

The comparison of test and FEA results for the horizontal connection specimen under shear load, illustrated in **Fig. 19**, demonstrates close agreement between the FE analysis and experimental observations. The load-deformation curves derived from both experimental and FEA methods exhibit a high degree of similarity, indicating a nearly identical response in both approaches. The FE model estimated an ultimate

shear load of 327.33 kN, compared to the experimentally derived value of 316.48 kN, yielding a minimal discrepancy of approximately 3.43%. Furthermore, the experimental displacement at failure was observed to be 6.03 mm, which slightly differs from the 6.09 mm predicted by the FEA, resulting in a deviation of about 1.00%.

**Fig. 26** presents the FEA results of Von Mises stresses and the failure mode of the horizontal connection specimen under shear load. The predicted failure location of the shear pins, specifically at the threaded connection with the roof node, closely matched experimental observations. Additionally, the circular hole at the bottom center of the floor node showed signs of plastic deformation as the Von Mises stress exceeded the material yield threshold, consistent with the experimental finding of distortion in the floor node's hole.

The Von Mises yield criterion, combined with the Multilinear Isotropic Hardening material model used in this study, assumes that once the material stress exceeds its ultimate strength, the stress remains constant while strain continues to increase. This limitation restricts ANSYS's ability to accurately simulate material fracture. Consequently, the complete failure of the shear pins could not be explicitly modeled. Instead, shear pin failure was inferred from the sudden drop in reaction force on the load-displacement curve and the visible deformation in the model, highlighting the limitations of this approach in fracture simulation.

### 5.4. Parametric study

This section examines the factors influencing the performance of vertical connection specimens under axial tensile and compression loads, and horizontal connection specimens under shear load. **Table 3**

**Table 3**  
Values of the parameters.

No	Specimen	Parameter	Values
1	Vertical connection	Roof node top plate's thickness	13 mm, 14 mm, 15 mm, 16 mm
2	Horizontal connection	Shear pin diameter	20 mm, 24 mm, 26 mm, 28 mm, 30 mm

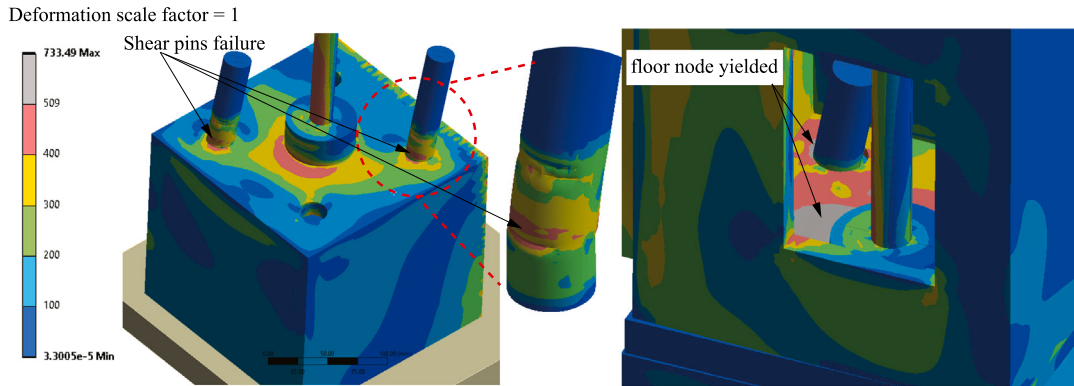


Fig. 26. FEA results of Von-Mises stresses and failure mode of the horizontal connection specimen under shear load.

lists the parameters selected for the parametric study, showing that nine different FE models were considered.

#### 5.4.1. Vertical connection specimen under axial tension and compression loads

Using FE models validated with experimental outcomes, a parametric study was undertaken to evaluate the effect of the top plate thickness of the roof node on the tensile and compressive capacities of the vertical connection. It is noteworthy that the thickness of the top plate of the roof node in the original specimen was 15 mm.

Figs. 27(a) and 27(b) demonstrate the relationship between changes in the top thickness of the roof node and the axial tensile and compressive load–displacement behaviors of the vertical connection. The figures indicate that as the thickness of the top roof node increases, there is a corresponding increase in both the yield load and the ultimate load under both tension and compression.

Fig. 27(c) depicts the ultimate tensile and compressive loads of the FE model as the thickness of the top roof nodes varies from 13 mm to 16 mm. It is observed that with a 3 mm increase in the thickness of the top roof nodes, the ultimate tensile and compressive ultimate loads of the vertical connection increased by 16.69% and 20.37%, respectively. The relationship between the node thickness and the ultimate tensile and compression load capacities of the vertical connection was almost linear, as indicated by R-square values of 0.986 and 0.957, respectively.

#### 5.4.2. Horizontal connection specimen under shear load

Employing FE models validated by experimental results, a parametric analysis was performed to investigate the influence of shear pin diameter on the maximum shear load capacity of the horizontal connection. It should be noted that in the initial specimen, the diameter of each of the two shear pins was 24 mm.

Fig. 28(a) demonstrates the relationship between changes in the diameter of the shear pins and the load–displacement behaviors of the horizontal connection. It is evident that increasing the diameter of the shear pins slightly increased the stiffness of the horizontal connection. Fig. 28(b) shows the ultimate shear loads predicted by the FE models as the diameter of the shear pins varies from 20 mm to 30 mm. A 10 mm increase in the diameter of the shear pins resulted in only a 4.37% increase in the shear-resistant capacity of the horizontal connection. This indicates that enlarging the diameter of the shear pins led to a modest enhancement in the ultimate shear load of the horizontal

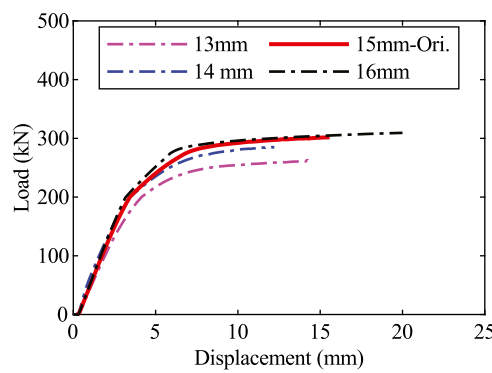
connections. Also, the relationship between the ultimate shear loads of the horizontal connection and the diameter of the shear pins was nearly linear, as shown by an R-square value of 0.860.

## 6. Conclusion

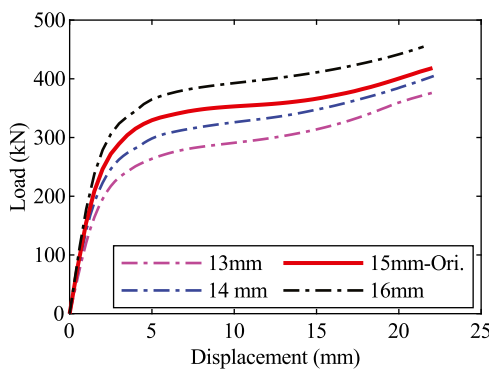
This study introduces a novel modular construction approach utilizing the Samsung Connection Node (S-CN) cast-steel connector in combination with RHS members. Comprehensive experimental evaluations were conducted to assess the S-CN connector's performance under horizontal shear forces and vertical axial tension and compression forces. While these findings provide valuable insights, they are limited to the context and scope of this study. The key conclusions are as follows:

- The vertical connection achieved a peak axial tension of 290.74 kN, failing due to upper node deformation and sleeve detachment. It withstood a compression load of 450.32 kN but ultimately failed due to deformation of the roof node and sleeve penetration. The horizontal connection sustained a shear load of 316.48 kN, with failure attributed to shear pin failure.
- The vertical connection's tensile and compressive performance was primarily influenced by the thickness of the roof node's top plate. Openings in the roof node reduced compression performance but had minimal impact on tension performance. Increasing the plate thickness from 13 mm to 16 mm improved tensile and compressive loads by 16.69% and 20.37%, respectively. For horizontal connections, increasing shear pin diameter modestly enhanced ultimate shear load, with a near-linear relationship observed.
- Experimental results closely aligned with Finite Element Analysis (FEA) predictions, with discrepancies in ultimate load and displacement ranging from 1% to 8%, validating the reliability of the FEA model.

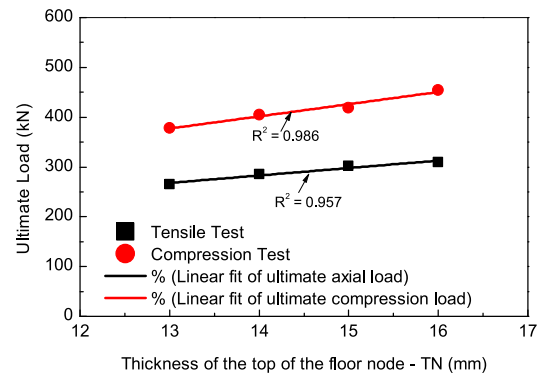
While the S-CN system demonstrates significant mechanical advantages and ease of assembly, key challenges include the lack of standardized design procedures and the need for further evaluation under seismic loads. Addressing these challenges is critical for large-scale implementation. Future research will focus on investigating the seismic performance of S-CN connections to further refine this modular construction system.



(a) Tension load - displacement behavior

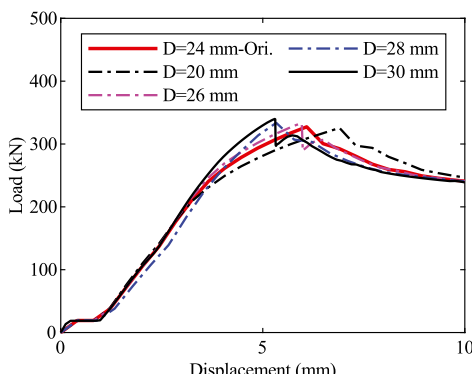


(b) Compression load - displacement behavior.

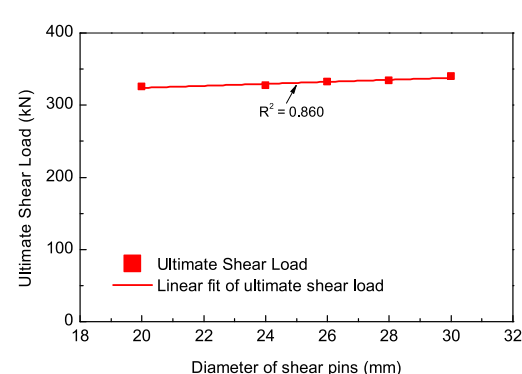


(c) Ultimate loads.

Fig. 27. Influence of roof node top thickness on ultimate compressive load and ultimate tensile load of the vertical connection.



(a) Load - displacement behavior



(b) Shear ultimate loads.

Fig. 28. Influence of shear pin diameter on ultimate shear load of the horizontal Connection.

**CRediT authorship contribution statement**

**Tran-Van Han:** Writing – review & editing, Writing – original draft, Validation, Software, Methodology, Formal analysis, Data curation, Conceptualization. **MoonSook Jeong:** Writing – review & editing, Formal analysis. **YongNam Kim:** Writing – review & editing, Formal analysis. **Dongkyu Lee:** Writing – review & editing, Formal analysis. **Nguyen Huu Cuong:** Validation, Software, Data curation. **Kihak Lee:** Writing – review & editing, Supervision, Resources, Project administration, Formal analysis.

**Declaration of competing interest**

The authors declare that they have no known competing financial interests or personal relationships that could have appeared to influence the work reported in this paper.

**Acknowledgments**

This study was completed with financial and technical assistance of Samsung C&T Corp. located in Seoul, Republic of Korea. This research was also funded by Ministry of Land, Infrastructure and Transport of Korean Government (RS-2024-00410886).

## Appendix. A Python program for generating input for the multi-linear isotropic hardening model in ANSYS

```

"""
@author: Han
"""

import numpy as np
import matplotlib.pyplot as plt

# Create multilinear hardening data for SCW550 steel
# Units: N, mm, MPa

# Material properties
E = 205000 # Young's modulus (MPa)
sigma_y = 509 # Engineering yield strength (MPa)
sigma_u = 649 # Engineering ultimate strength (MPa)
epsilon_y = 0.17 / 100 # Yield strain (%)
epsilon_sh = max(0.015, min(0.1 * (sigma_y / sigma_u) - 0.055, 0.03)) # Clamping strain for
#hardening
epsilon_u = max(0.6 * (1 - sigma_y / sigma_u), 0.06) # Ultimate strain (%)

# Data points for plotting
n = 10 # Elastic
m = 6 # Yield
k = 11 # Hardening

# Elastic stage
epsilon_elastic = np.linspace(0, epsilon_y, n)
sigma_elastic = E * epsilon_elastic
epsilon_elastic = epsilon_elastic[:-1] # Avoid duplicate at yield point
sigma_elastic = sigma_elastic[:-1]

# Yield stage
epsilon_yield = np.linspace(epsilon_y, epsilon_sh, m)
sigma_yield = sigma_y * np.ones_like(epsilon_yield)
epsilon_yield = epsilon_yield[:-1] # Avoid duplicate at hardening point
sigma_yield = sigma_yield[:-1]

# Hardening stage
epsilon_hardening = np.linspace(epsilon_sh, epsilon_u, k)
relative_hardening = (epsilon_hardening - epsilon_sh) / (epsilon_u - epsilon_sh)
hardening_factor = (1 + 400 * relative_hardening**5)**(1/5)
sigma_hardening = sigma_y + (sigma_u - sigma_y) * (0.4 * relative_hardening + 2 *
relative_hardening / hardening_factor)

# Combine all stages
epsilon_combined = np.concatenate((epsilon_elastic, epsilon_yield, epsilon_hardening))
sigma_combined = np.concatenate((sigma_elastic, sigma_yield, sigma_hardening))

# Plot combined engineering stress-strain curve
plt.figure()
plt.plot(epsilon_combined, sigma_combined)
plt.title('Engineering stress-strain curve of SCW550')
plt.xlabel('Strain (mm/mm)')
plt.ylabel('Stress (MPa)')
plt.show()

# True stress-strain calculation
true_epsilon = np.log(1 + epsilon_combined)
true_sigma = sigma_combined * (1 + epsilon_combined)

# Plot true stress-strain curve
plt.figure()
plt.plot(true_epsilon, true_sigma)
plt.title('True stress-strain curve of SCW550')
plt.xlabel('Strain (mm/mm)')
plt.ylabel('Stress (MPa)')
plt.show()

# Plastic strain computation

```

```

elastic_strain = true_sigma / E
plastic_strain = np.abs(true_epsilon - elastic_strain)

# Prepare data for export to ANSYS
plastic_strain_input = plastic_strain[n-1:] # Start from last elastic point
plastic_stress_input = true_sigma[n-1:]
stress_strain_input = np.column_stack((plastic_strain_input, plastic_stress_input))

# Export data to Excel
import pandas as pd
filename = 'stress_strain_curve_input_ANSYS_SCW550.xlsx'
pd.DataFrame(stress_strain_input, columns=['Plastic Strain', 'Plastic Stress']).to_excel(filename,
index=False)

```

## References

- [1] Thai H-T, Ngo T, Uy B. A review on modular construction for high-rise buildings. In: Structures, vol. 28. Elsevier; 2020, p. 1265–90. <http://dx.doi.org/10.1016/j.istruc.2020.09.070>.
- [2] Modular D. The differences between prefab and modular construction. 2019, URL <https://www.deluxmodular.com/learning-center/modular-vs-prefab>.
- [3] Yu Y, Chen Z. Rigidity of corrugated plate sidewalls and its effect on the modular structural design. Eng Struct 2018;175:191–200. <http://dx.doi.org/10.1016/j.engstruct.2018.08.039>.
- [4] Jin R, Hong J, Zuo J. Environmental performance of off-site constructed facilities: a critical review. Energy Build. 2020;207:109567. <http://dx.doi.org/10.1016/j.enbuild.2019.109567>.
- [5] Civera M, Surace C. Instantaneous spectral entropy: An application for the online monitoring of multi-storey frame structures. Buildings 2022;12(3):310. <http://dx.doi.org/10.3390/buildings12030310>.
- [6] Lacey AW, Chen W, Hao H, Bi K. Structural response of modular buildings—an overview. J Build Eng 2018;16:45–56. <http://dx.doi.org/10.1016/j.jobe.2017.12.008>.
- [7] Srisangeerthanan S, Hashemi MJ, Rajeev P, Gad E, Fernando S. Review of performance requirements for inter-module connections in multi-story modular buildings. J Build Eng 2020;28:101087. <http://dx.doi.org/10.1016/j.jobe.2019.101087>.
- [8] Chen Z, Li H, Chen A, Yu Y, Wang H. Research on pretensioned modular frame test and simulations. Eng Struct 2017;151:774–87. <http://dx.doi.org/10.1016/j.engstruct.2017.08.019>.
- [9] Sanches R, Mercan O, Roberts B. Experimental investigations of vertical post-tensioned connection for modular steel structures. Eng Struct 2018;175:776–89. <http://dx.doi.org/10.1016/j.engstruct.2018.08.049>.
- [10] Liew J, Chua Y, Dai Z. Steel concrete composite systems for modular construction of high-rise buildings. In: Structures, vol. 21. Elsevier; 2019, p. 135–49. <http://dx.doi.org/10.1016/j.istruc.2019.02.010>.
- [11] Dai Pang S, Liew JRL, Dai Z, Wang Y. Prefabricated prefinished volumetric construction joining techniques review. 2016.
- [12] Lacey AW, Chen W, Hao H, Bi K, Tallowin FJ. Shear behaviour of post-tensioned inter-module connection for modular steel buildings. J Constr Steel Res 2019;162:105707. <http://dx.doi.org/10.1016/j.jcsr.2019.105707>.
- [13] Lacey AW, Chen W, Hao H, Bi K. Review of bolted inter-module connections in modular steel buildings. J Build Eng 2019;23:207–19. <http://dx.doi.org/10.1016/j.jobe.2019.01.035>.
- [14] Deng E-F, Zong L, Ding Y, Dai X-M, Lou N, Chen Y. Monotonic and cyclic response of bolted connections with welded cover plate for modular steel construction. Eng Struct 2018;167:407–19. <http://dx.doi.org/10.1016/j.engstruct.2018.04.028>.
- [15] Deng E-F, Yan J-B, Ding Y, Zong L, Li Z-X, Dai X-M. Analytical and numerical studies on steel columns with novel connections in modular construction. Int J Steel Struct 2017;17:1613–26. <http://dx.doi.org/10.1007/s13296-017-1226-5>.
- [16] Chen Z, Liu J, Yu Y. Experimental study on interior connections in modular steel buildings. Eng Struct 2017;147:625–38. <http://dx.doi.org/10.1016/j.engstruct.2017.06.002>.
- [17] Chen Z, Liu J, Yu Y, Zhou C, Yan R. Experimental study of an innovative modular steel building connection. J Constr Steel Res 2017;139:69–82. <http://dx.doi.org/10.1016/j.jcsr.2017.09.008>.
- [18] Cho B-H, Lee J-S, Kim H, Kim D-J. Structural performance of a new blind-bolted frame modular beam-column connection under lateral loading. Appl Sci 2019;9(9):1929. <http://dx.doi.org/10.3390/app9091929>.
- [19] Lacey AW, Chen W, Hao H, Bi K. New interlocking inter-module connection for modular steel buildings: Experimental and numerical studies. Eng Struct 2019;198:109465. <http://dx.doi.org/10.1016/j.jCSR.2019.109465>.
- [20] Lee S, Park J, Shon S, Kang C. Seismic performance evaluation of the ceiling-bracket-type modular joint with various bracket parameters. J Constr Steel Res 2018;150:298–325. <http://dx.doi.org/10.1016/j.jCSR.2018.08.008>.
- [21] Lee SS, Bae KW, Park KS, Hong SY. An experimental evaluation of structural performance for the beam to column joints in unit modular system. J Kor Soc Steel Construct 2013;25(3):255–65. <http://dx.doi.org/10.7781/kjoss.2013.25.3.255>.
- [22] Sendanayake S, Thambiratnam D, Perera N, Chan T, Aghdamy S. Enhancing the lateral performance of modular buildings through innovative inter-modular connections. In: Structures, vol. 29. Elsevier; 2021, p. 167–84. <http://dx.doi.org/10.1016/j.istruc.2020.10.047>.
- [23] Sendanayake SV, Thambiratnam DP, Perera N, Chan T, Aghdamy S. Seismic mitigation of steel modular building structures through innovative inter-modular connections. Heliyon 2019;5(11):e02751. <http://dx.doi.org/10.1016/j.heliyon.2019.e02751>.
- [24] Sharafi P, Mortazavi M, Samali B, Ronagh H. Interlocking system for enhancing the integrity of multi-storey modular buildings. Autom Construct 2018;85:263–72. <http://dx.doi.org/10.1016/j.autcon.2017.10.023>.
- [25] Dhanapal J, Ghaednia H, Das S, Veloci J. Structural performance of state-of-the-art VectorBloc modular connector under axial loads. Eng Struct 2019;183:496–509. <http://dx.doi.org/10.1016/j.engstruct.2019.01.023>.
- [26] Kalam L, Dhanapal J, Das S, Ghaednia H. Behavior of vectorbloc beam-column connections. In: Proceedings of the Canadian society of civil engineering annual conference 2021: CSCE21 general track volume 2. Springer; 2022, p. 333–44.
- [27] Hajimohammadi B, Das S, Ghaednia H, Dhanapal J. Structural performance of registration pin connection in VectorBloc modular construction system. J Constr Steel Res 2022;197:107464. <http://dx.doi.org/10.1016/j.jCSR.2022.107464>.
- [28] Doh JH, Ho NM, Miller D, Peters T, Carlson D, Lai P. Steel bracket connection on modular buildings. J Steel Struct Construct 2017;2(02). <http://dx.doi.org/10.4172/2472-0437.1000121>, 2472–0437.
- [29] Chen Z, Liu Y, Zhong X, Liu J. Rotational stiffness of inter-module connection in mid-rise modular steel buildings. Eng Struct 2019;196:109273. <http://dx.doi.org/10.1016/j.engstruct.2019.06.009>.
- [30] Dai X-M, Zong L, Ding Y, Li Z-X. Experimental study on seismic behavior of a novel plug-in self-lock joint for modular steel construction. Eng Struct 2019;181:143–64. <http://dx.doi.org/10.1016/j.jCSR.2018.11.075>.
- [31] Deng E-F, Lian J-Y, Liu Z, Zhang G-C, Wang S-B, Cao D-B. Compressive behavior of a fully prefabricated liftable connection for modular steel construction. Buildings 2022;12(5):649. <http://dx.doi.org/10.3390/buildings12050649>.
- [32] Deng E-F, Wang Y-H, Zong L, Zhang Z, Zhang J-F. Seismic behavior of a novel liftable connection for modular steel buildings: Experimental and numerical studies. Thin-Walled Struct 2024;197:111563. <http://dx.doi.org/10.1016/j.tws.2024.111563>.

- [33] Deng E-F, Lian J-Y, Zhang Z, Qian H, Zhang G-C, Zhang P, Sheikh SA. Axial mechanical behavior of an innovative liftable connection for modular steel construction. *Thin-Walled Struct* 2023;182:110256. <http://dx.doi.org/10.1016/j.tws.2022.110256>.
- [34] Fadden M, McCormick J. Cyclic quasi-static testing of hollow structural section beam members. *J Struct Eng* 2012;138(5):561–70. [http://dx.doi.org/10.1061/\(ASCE\)ST.1943-541X.00005](http://dx.doi.org/10.1061/(ASCE)ST.1943-541X.00005).
- [35] Han T-V, MoonSook J, Kim Y, Lee D, Luat N-V, Lee K. Numerical study on compressive behavior of a 3D-printed sand mold-cast S-CN connector. *J Constr Steel Res* 2024;213:108336. <http://dx.doi.org/10.1016/j.jcsr.2023.108336>.
- [36] Lee D-Y, Cho B-H, Jung D-I, Choi J-Y, Lee J-S, Cho K-H, Park J-K, Shin M-G. Connecting performance evaluation of the Quick-Connector for modular steel construction. *Eng Struct* 2024;299:117126. <http://dx.doi.org/10.1016/j.engstruct.2023.117126>.
- [37] Waters Jr. W, Williams JG. Failure mechanisms of laminates transversely loaded by bolt push-through. 1985.
- [38] ANSYS. ANSYS theory reference. 2021, Canonsburg, PA, USA: Ansys.
- [39] Yun X, Gardner L. Stress-strain curves for hot-rolled steels. *J Constr Steel Res* 2017;133:36–46. <http://dx.doi.org/10.1016/j.jcsr.2017.01.024>.
- [40] Standard B. Eurocode 3—Design of steel structures—. BS EN 1993-1 2006;1:2005.
- [41] EN C. 1-5: Eurocode 3—Design of steel structures—Part 1-5: Plated structural elements. 2006, CEN: Brussels, Belgium.
- [42] ANSYS. ANSYS Mechanical APDL Material Reference. ANSYS Inc; 2013.
- [43] ANSYS. ANSYS mechanical APDL element reference guide. Ansys Inc Canonsburg, PA; 2020.
- [44] 1090-2 E. Execution of steel structures and aluminium structures. Part 2. technical requirements for steel structures. CEN-European Committee For Standardization; 2018.
- [45] Alexander E. Analysis and design of threaded assemblies. *SAE Trans* 1977;86:1838–52, URL <http://www.jstor.org/stable/44644510>.
- [46] Grimsmo E, Aalberg A, Langseth M, Clausen A. Failure modes of bolt and nut assemblies under tensile loading. *J Constr Steel Res* 2016;126:15–25. <http://dx.doi.org/10.1016/j.jcsr.2016.06.023>.